optica

Direct imaging of hybridized eigenmodes in coupled silicon nanoparticles

JORIK VAN DE GROEP, TOON COENEN, SANDER A. MANN, AND ALBERT POLMAN*

Center for Nanophotonics, FOM Institute AMOLF, Science Park 104, 1098 XG Amsterdam, The Netherlands
**Corresponding author: polman@amolf.nl*

Received 6 November 2015; accepted 4 December 2015 (Doc. ID 253372); published 14 January 2016

High-index dielectric nanoparticles support leaky geometrical resonances in the visible spectral range with large interaction cross sections, and find applications in nanoscale optoelectronic devices and surface coatings. Coupling between such resonant nanoparticles in close proximity can give rise to enhanced directionality and confinement. Here, we combine dark-field (DF) scattering spectroscopy with cathodoluminescence (CL) imaging spectroscopy to study hybridization of resonant modes in coupled silicon nanoparticles and directly image the modal field profiles of these hybridized eigenmodes. The DF measurements show a strong influence of the gap size on the scattering spectrum as a result of hybridization. Using finite-element modeling we calculate the eigenmodes of the dimer and identify the hybridized eigenmodes in the scattering spectrum. CL imaging spectroscopy is used to directly map the modal field profiles of single particles and dimer structures with deep-subwavelength spatial resolution. Detailed comparison with eigenmode calculations shows that the measured modal field profiles correspond to the hybridized symmetric electric and antisymmetric magnetic bonding modes. We study dimers composed of large dielectric bars to explore the ability of CL imaging to map highly complex hybridized field profiles inside resonant nanostructures. Our results demonstrate the ability to characterize the complex resonant properties of coupled nanostructures, paving the way for more complex applications and devices based on resonant dielectric nanoparticles.

OCIS codes: (290.5850) Scattering, particles; (180.5810) Scanning microscopy; (350.4238) Nanophotonics and photonic crystals.

http://dx.doi.org/10.1364/OPTICA.3.000093

1. INTRODUCTION

Dielectric nanostructures with a high refractive index exhibit geometrical resonances that allow for strong scattering and confinement of light at the nanoscale [1–3]. These properties have resulted in widespread application of dielectric resonators in nanoscale or nanopatterned devices, including photodetectors [4,5], lasers [6–8], and solar cells [9–12]. High-index dielectric particles support both electric and magnetic modes in the visible and near-IR spectral range [1,13–16]. Interference between the magnetic dipolar (MD) and electric dipolar (ED) modes can be used to engineer strongly directional scattering profiles [17–19], and realize all-dielectric low-loss metamaterials [20–23] and metasurfaces [24,25].

To fully exploit the potential of dielectric resonators in more complex structures and devices, a fundamental understanding of the resonant properties of individual nanoparticles is essential. Recently, we used cathodoluminescence (CL) imaging spectroscopy to study the resonant properties of single Si nanoparticles [26]. Using the high spatial resolution of CL, we systematically mapped the resonant modes in single silicon nanocylinders as a function of particle diameter. Here, we study how resonant particles that are placed in close proximity interact and how their resonant modes are modified.

Recently, coupled dielectric resonators have attracted widespread attention due to their ability to enhance the scattering directionality and concentration of light compared to a single particle. For example, Si dimers and trimers are known to exhibit strongly directional scattering as a result of coupled resonances [27,28]. Furthermore, electric and magnetic field enhancements in the gap of dielectric dimers have been studied theoretically [27,29] and demonstrated experimentally [30]. Similar to the hybridization of electric modes in plasmonic dimers [31,32], coupling between electric and magnetic dipolar modes in dielectric resonators can give rise to hybridization, resulting in symmetric and antisymmetric bonding modes [29,33]. The hybridization of ED and MD modes in Si spheres on glass has been studied experimentally using dark-field (DF) spectroscopy [33]. Despite the fact that DF spectroscopy gives spectral information on scattering by hybridized resonant modes, it does not give any insight into the hybridized spatial field profiles. Scanning near-field optical microscopy (SNOM) has been used to map hybridized field profiles in plasmonic dimers, where the electromagnetic fields are primarily localized on the surface of the nanostructures [34]. For dielectric particles, on the other hand, the fields are mainly concentrated inside the nanoparticles, giving rise to a reduced near-field intensity [29]. Although SNOM can be used to map

2334-2536/16/010093-07$15/0$15.00 © 2016 Optical Society of America

the local field enhancements [30], it is unable to map the hybridized modal field profiles inside the particles.

Here, we combine DF spectroscopy with CL imaging spectroscopy to directly image the field profiles of the hybridized eigenmodes *inside* coupled Si nanoparticles. We fabricate both isolated and coupled Si cubes instead of spheres to reduce the effective gap size and thereby enhance the interparticle coupling. Using DF spectroscopy, we study the influence of gap size on the scattering spectrum and show strong spectral splitting as a result of mode hybridization. We use finite-element modeling to calculate the eigenmodes of the single cubes and dimers, and identify the hybridized eigenmodes. Next, we use CL imaging to directly map the field profiles of the isolated particles and hybridized modes in coupled nanoparticles. Finally, we image the field profiles of larger rectangular dimers and map the complex hybridization modes with deep-subwavelength resolution.

2. FABRICATION

Single crystalline Si cubes and dimers with spacing in the range of 0–100 nm were fabricated on a thin SiO_2 layer, supported by a thick Si wafer. Starting with a silicon-on-insulator wafer (100 nm Si layer and 300 nm SiO_2 layer on a Si substrate), the top layer was patterned into nanostructures. First, electron beam lithography was used to write squares and dimers into a negative-tone electron beam resist to form an etch mask. Second, the pattern was etched into the Si top layer using anisotropic reactive-ion etching. Third, the etch mask was removed using a short wet etch in hydrofluoric (HF) acid. See Supplement 1 for the details of the fabrication process.

The resulting Si cubes are 90 nm wide, 100 nm tall, and have rounded edges. Figure 1 shows scanning electron micrographs (SEMs) of the particles [Fig. 1(a)] and of a focused ion beam (FIB) cross section [Fig. 1(b)] of the resulting dimer. A protective layer of Pt was deposited using electron-beam-induced deposition to improve the quality of the FIB cross section. The cubical shape of the individual nanoparticles is clearly visible. Furthermore, a small underetch of the SiO_2 layer as a result of the HF etch can be observed. The dimers were spaced 5 μm apart, such that experiments could be performed on isolated particles and dimers.

3. DF SPECTROSCOPY

To study the hybridization of the eigenmodes, we start by using optical DF backscattering spectroscopy to measure the scattering spectra of the single particles and the dimers with different particle spacing. Single particles and dimers were illuminated with unpolarized white light, and scattered light in the 430–570 nm spectral range was collected by a 100 × microscope objective (0.9 NA) and analyzed using a spectrograph with a CCD camera (see Supplement 1 for experiment details). Figure 2 shows the DF spectra and corresponding SEM images for a single particle (blue), and for dimers with a spacing of 100 nm (green), 25 nm (yellow), and 0 nm (orange). The spectra for a rectangle (red) and the flat substrate next to the particles (gray) are also shown for reference.

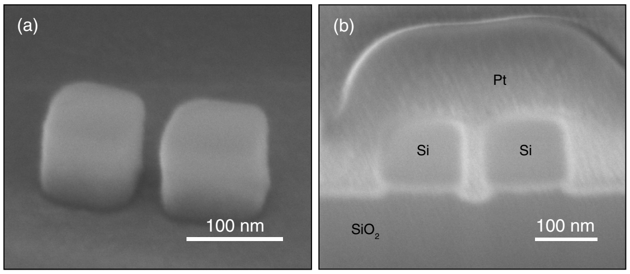

Fig. 1. (a) SEM image of Si dimer on oxide layer (imaged under 52°), (b) FIB cross section of the Si dimer, showing the rounded square shape of the particles and the small underetch. The different layers are labeled. The particles are surrounded by Pt, which is deposited to improve the quality of the FIB cross section.

Two clear resonant peaks at $\lambda = 430$ nm and $\lambda = 485$ nm can be observed for the single particle. These peaks originate from resonant scattering by the in-plane MD ($\lambda = 485$ nm) and in-plane ED ($\lambda = 430$ nm) modes [15,29,30,33,35]. These modes are degenerate in both in-plane directions as a result of symmetry. For a dimer with spacing sp = 100 nm, defined as the size of the gap between particles, the scattering spectrum strongly resembles that of the single particle, which indicates the lack of coupling. However, the resonance wavelengths strongly shift when the spacing is reduced to 25 nm. The peak at $\lambda = 485$ nm broadens into two separate peaks, which indicates hybridization of the localized modes [33]. A small redshift to $\lambda = 435$ nm is observed for the ED mode, and the MD mode broadens into two modes at $\lambda = 480$ nm and $\lambda = 495$ nm as a result of hybridization, leading to a 5 nm blueshift and 10 nm redshift compared to the single-particle spectrum, respectively. A drastic transformation of the scattering spectrum is observed as the particles physically connect (sp = 0 nm, orange). The lowest energy mode strongly redshifts, and higher-order modes appear. These correspond to the resonant modes of the new structure formed by the touching cubes, which is confirmed by the strong resemblance to the scattering spectrum of the rectangle (red).

To explain the origin of the splitting observed for 25 nm spacing (yellow spectrum in Fig. 2), we use finite-element

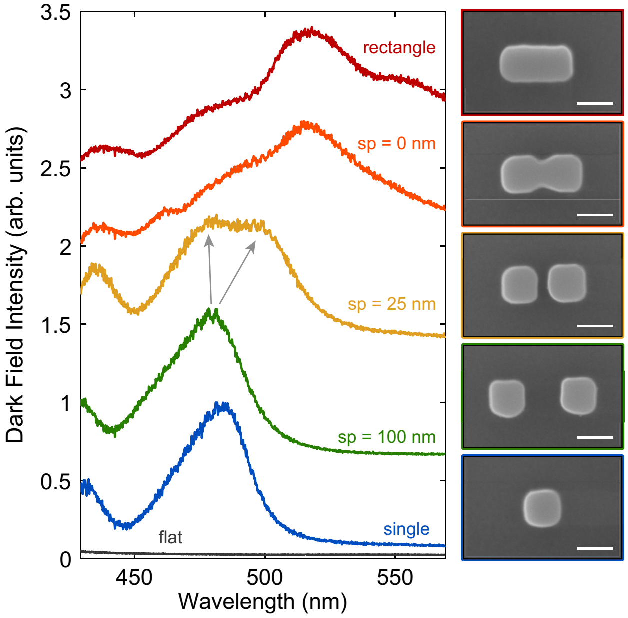

Fig. 2. Dark-field scattering spectra for a single square (blue), dimers with various spacing, and a rectangle (red). The spectrum for the flat background is also shown (gray). Note that each spectrum is normalized to 1 separately and displayed with a vertical offset for visibility. SEM images of the corresponding particles taken at normal incidence are shown on the right. The scale bar in all images is 100 nm.

calculations [36] to find the eigenmodes of the dimer structure. We assume the cubes are nondispersive and lossless with $\epsilon_r = 20$, and neglect the substrate. Although a multilayer substrate can significantly modify the line width [37] and excitation efficiency of modes [35], the influence of the substrate on the eigenmode field profile was found to be minor. Note that due to these assumptions, the calculated eigenfrequencies do not directly match the measured resonance wavelengths. See Supplement 1 for details on the finite-element calculations.

We focus on the coupling between the in-plane MD modes, and assume that the DF illumination does not introduce any asymmetry. As a result, only symmetric modes that can be excited by incident plane waves are considered. This assumption has been demonstrated to accurately describe DF scattering spectra of hybridized spherical Si particles on a glass substrate [33]. Under these conditions, two hybridized bonding modes are found that both can be excited directly by incident plane waves. Figures 3(a) and 3(b) show schematic representations of the symmetric $m_x - m_x$ and symmetric $m_y - m_y$ bonding modes, respectively, where m_i represents a magnetic dipole moment along the i axis. Note that (anti)symmetric modes refer to (anti)parallel orientation of the dipole moments. The retrieved eigenfrequencies are $f_{m_x - m_x} = (561 + 19i)$ THz ($Q \sim 30$) and $f_{m_y - m_y} = (579 + 31i)$ THz ($Q \sim 19$). The large imaginary part indicates that these modes exhibit strong radiative damping. The spectral spacing between the calculated eigenmodes is 16.5 nm, which corresponds well to the experimentally observed splitting in Fig. 2. To corroborate the magnetic nature of the hybridized eigenmodes, Figs. 3(c)–3(f) show in-plane (x–y) cross cuts of the electric field intensity [Figs. 3(c) and 3(d)] and magnetic field intensity [Figs. 3(e) and 3(f)] inside the particles. The spots of high electric field intensity on either side of the particles in Figs. 3(c) and 3(d) correspond to cross cuts of the displacement current loops, which are characteristic of in-plane MD modes. Furthermore, high magnetic field intensities can be observed in the center of the particles [Figs. 3(e) and 3(f)] as a result of the magnetic dipole moment. Finally, the blueshift of the symmetric $m_y - m_y$ bonding mode ($\lambda = 480$ nm) and redshift of the symmetric $m_x - m_x$ bonding mode ($\lambda = 495$ nm) with respect to the single-particle spectrum ($\lambda = 485$ nm) are in agreement with theoretical predictions [29] and DF scattering measurements of spherical dimers [33].

Interestingly, the peak corresponding to the symmetric $p_x - p_x$ bonding mode is not clearly visible in the scattering spectrum (Fig. 2). This mode has been shown to redshift and significantly broaden compared to the single-particle p_x mode due to enhanced radiative damping, effectively covering the entire experimental spectral range. We attribute the remaining peak at $\lambda = 435$ nm to the symmetric $p_y - p_y$ bonding mode, which can be distinguished using polarization-resolved DF scattering spectroscopy [33].

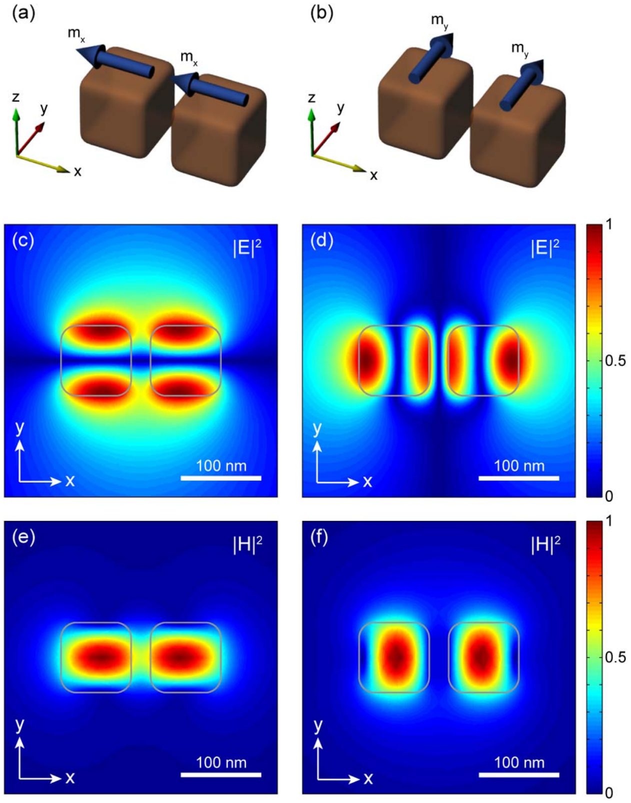

Fig. 3. Schematic of the (a) symmetric $m_x - m_x$ bonding mode and (b) symmetric $m_y - m_y$ bonding mode. (c)–(f) In-plane cross cuts (x–y plane) through the middle of dimers showing the electric field intensity [(c), (d)] and magnetic field intensity [(e), (f)] of the symmetric $m_x - m_x$ bonding mode [(c), (e)] and symmetric $m_y - m_y$ bonding mode [(d), (f)]. The particle contours are also shown (gray). The calculated eigenfrequencies are $f_{m_x - m_x} = (561 + 19i)$ THz and $f_{m_y - m_y} = (579 + 31i)$ THz.

4. CATHODOLUMINESCENCE SPECTROSCOPY

After the observation of hybridization in the DF scattering spectra, we use CL imaging spectroscopy to study the resonant modes in more detail. CL spectroscopy uses a focused 30 keV electron beam in a scanning electron microscope as a broadband light source to locally excite the sample [38,39]. The high spatial resolution of the source allows for deep-subwavelength mapping of the optical modes [40], and has been used to study resonant modes in both metallic [41–45] and dielectric [26,40] nanophotonic structures. Furthermore, the electron beam is an azimuthally symmetric point source that primarily couples to the vertical component of the electric field [46], which allows for the excitation of eigenmodes that are difficult to excite with plane waves due to the antisymmetric character of their mode profiles (i.e., symmetric charge distribution). Similar to the results obtained for single Si nanocylinders [26], this experimental technique allows for spatial and spectral mapping of the resonant modes inside our Si dimers. Here, we apply this technique to directly image the field profiles of hybridized eigenmodes.

A. Single Particle

Before considering the dimers in CL, we first study the resonant modes of a single Si cube. In the experiment, we scan the electron beam over the sample in 8 nm steps and collect a full CL spectrum at each pixel. Next, the background originating from the substrate is subtracted, and we sum over the pixels corresponding to the particle to obtain the CL spectrum (see Supplement 1 for experiment details).

Figure 4(a) shows the CL spectrum for a single Si cube. Two clear peaks can be observed at $\lambda = 485$ nm and $\lambda = 430$ nm, and the shoulder of a third peak around $\lambda = 390$ nm. For $\lambda > 500$ nm, a high but flat background signal is observed, which is caused by imperfect subtraction of the large background signal

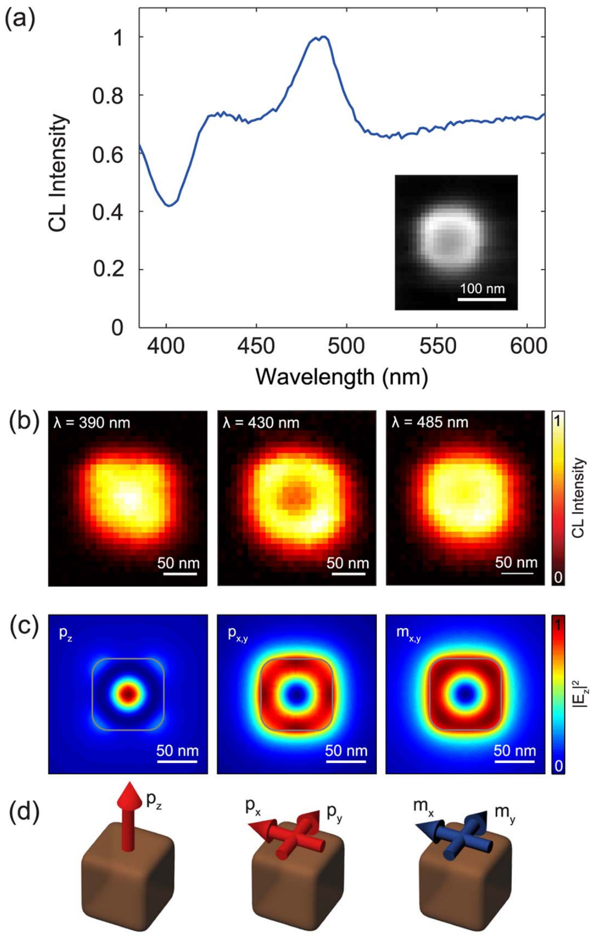

Fig. 4. (a) Normalized CL spectrum for a single square. The SEM image of the particle collected simultaneously with the CL spectrum is shown as an inset. (b) Two-dimensional CL intensity maps for resonant peaks in (a) at $\lambda = 390$ nm, $\lambda = 430$ nm, and $\lambda = 485$ nm, (c) $|E_z|^2$ of the vertical electric dipole (p_z, left), in-plane electric dipole (p_x, p_y, center), and in-plane magnetic dipole (m_x, m_y, right). The corresponding eigenfrequencies are $f_{p_z} = (826 + 52i)$ THz, $f_{p_{x,y}} = (807 + 35i)$ THz, and $f_{m_{x,y}} = (589 + 15i)$ THz. The profiles in (c) have been obtained by averaging over the two in-plane directions to account for degeneracy; the field for $p_{x,y}$ is plotted 25 nm above the center of the particle. (d) Schematic representations of the eigenmodes.

induced by defect luminescence in the SiO_2 layer. Note that the resonant wavelengths show excellent agreement with the DF scattering spectrum for the single particle (blue line in Fig. 2), which indicates the peaks at $\lambda = 485$ and 430 nm correspond to the in-plane MD and ED modes, respectively.

To characterize the spatial mode profile, Fig. 4(b) shows the two-dimensional CL intensity maps for wavelengths corresponding to all three resonant peaks. For $\lambda = 390$ nm, the CL intensity is the maximum in a bright spot in the center. For $\lambda = 430$ and 485 nm, on the other hand, a clear ring of maximum intensity is observed along the circumference of the particle, although the low intensity in the center of the ring is more pronounced for $\lambda = 430$ nm than for 485 nm.

To corroborate that the electron beam couples to the in-plane ED and MD modes, we calculated the eigenmodes for an individual cube and compared them to the CL intensity maps. Since the electron beam primarily couples to the vertical component of the electric fields [46], we now consider $|E_z|^2$ only, and not $|E|^2$. Three different eigenmodes are found for the single particle that can be excited by electron irradiation along the z axis [see Fig. 4(d) for schematics]. Figure 4(c) presents cross cuts along the x–y plane showing $|E_z|^2$ for the p_z mode (left), the degenerate $p_{x,y}$ mode (center), and the degenerate $m_{x,y}$ mode (right). Here, p_i refers to an electric dipole moment along the i axis. Note that the degeneracy is taken into account by averaging the modal intensity profiles over both orientations. Furthermore, note that $E_z = 0$ in the plane across the middle of the particle for $p_{x,y}$. For this reason, the cross cut is taken 25 nm above the center of the particle, where E_z is nonzero.

The bright spot in the center for $\lambda = 390$ nm is clearly reproduced by the field profile of the out-of-plane p_z mode, which has a higher eigenfrequency due to the asymmetry of the particle induced by the nonunity aspect ratio. Also, the rings of high intensity observed for $\lambda = 430$ nm and $\lambda = 485$ nm [Fig. 4(b)] are well reproduced by the E_z fields of the in-plane $p_{x,y}$ mode and in-plane $m_{x,y}$ mode, respectively. Altogether this confirms that the peaks at $\lambda = 430$ and 485 nm correspond to the in-plane ED and MD modes, respectively, and demonstrates that CL spectroscopy allows for systematic mapping of the modal field profiles inside the particles with deep-subwavelength resolution. Note that higher-order modes (e.g., electric and magnetic quadrupole) are also supported outside of our experimental spectral range.

B. Dimers

Next, we study coupled dimer structures. Figure 5 compares the normalized CL spectrum for a single cube (blue) with that for dimers with varying spacing and a rectangle (red). Analogous to the trends in the DF scattering spectra in Fig. 2, the CL spectrum for 100 nm spacing strongly resembles that of the single particle, which indicates weak coupling. However, for 25 nm spacing the CL spectrum changes drastically, showing a nearly flat high intensity for $\lambda > 430$ nm, which indicates efficient excita-

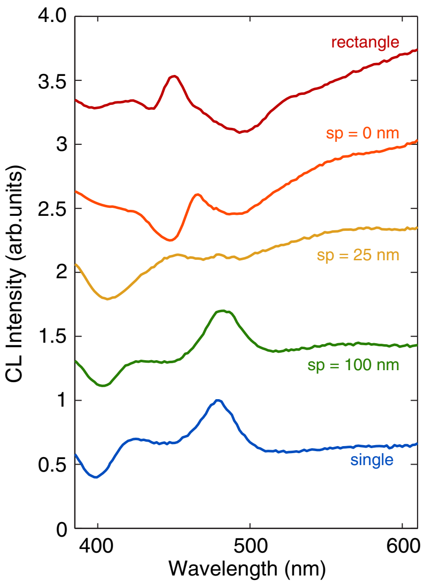

Fig. 5. CL intensity spectra for a single square (blue), dimers with various spacing, and a rectangle (red). Note that the spectra are vertically offset for visibility.

tion of a wide range of (hybridized) modes. Note that the electron beam also couples to antisymmetric eigenmodes, which were not considered for plane wave excitation in Fig. 2. For touching particles ($\mathrm{sp} = 0$), the lowest-order mode strongly redshifts to $\lambda \sim 530$ nm, and resonance peaks corresponding to higher-order modes occur. The resonant peaks observed for $\mathrm{sp} = 0$ are attributed again to the geometrical modes of a rectangle, which shows a very similar spectrum (red). The spectrum for $\mathrm{sp} = 0$ shows a small redshift with respect to that of the rectangle due to the slightly longer effective length of the touching cubes.

We now examine the spatial CL intensity maps of the hybridized modes for $\mathrm{sp} = 25$ nm. Due to the local excitation of the electron beam, both symmetric and antisymmetric combinations of the ED and MD modes are excited in the hybridized system, with large spectral overlap. As a result, the two-dimensional CL intensity maps are comprised of multiple (hybridized) eigenmodes. However, two dominant hybridized mode profiles are clearly visible. Figure 6(a) shows the spatial CL intensity maps for $\lambda = 450$ nm and $\lambda = 490$ nm. The strong asymmetry in the intensity profile of the individual dimer particles is a direct indication of hybridization, and well-defined modal field profiles can be observed in Fig. 6(a). For $\lambda = 450$ nm, high CL intensities are located at the outside of the dimer, whereas high intensities are located near the center of the dimer for $\lambda = 490$ nm [see Fig. 6(b) for cross cuts]. Note that for very small spacing, heterogeneous coupling (between ED and MD modes) may also play a role [33].

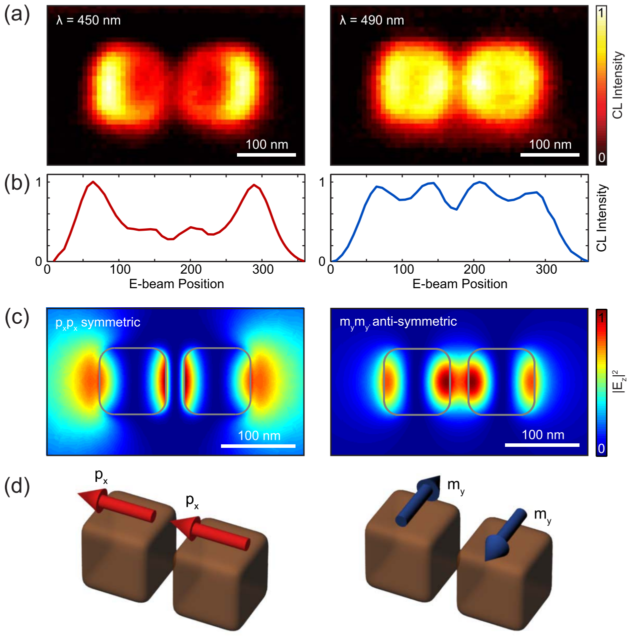

Fig. 6. (a) Two-dimensional CL intensity maps for $\lambda = 450$ nm (left) and $\lambda = 490$ nm (right) showing hybridized modal field profiles, (b) cross cuts through (a) showing the high field intensity on the outside (left) and inside (right) of the dimer, (c) cross cuts displaying $|E_z|^2$ for the symmetric $p_x - p_x$ bonding mode (left) and the antisymmetric $m_y - m_y$ bonding mode (right). The corresponding eigenfrequencies are $f_{p_x - p_x} = (728 + 148i)$ THz and $f_{m_y - m_{y'}} = (582 + 9i)$ THz. Note that the left cross cut is taken 25 nm above the center of the particle, as $E_z = 0$ in the center for $p_{x,y}$ modes. (d) Schematic representation of the hybridized dipolar modes.

To further study the hybridization observed in Fig. 6(a), we reconsider the calculated eigenmodes and compare them with the two-dimensional CL intensity maps. Figure 6(c) shows cross cuts of $|E_z^2|$ for the symmetric $p_x - p_x$ bonding mode (left) and the antisymmetric $m_y - m_{y'}$ bonding mode (right), where y' refers to the opposite orientation of y. The corresponding eigenfrequencies are $f_{p_x - p_x} = (728 + 148i)$ THz and $f_{m_y - m_{y'}} = (582 + 9i)$ THz, respectively. Schematic representations of the hybridized modes are shown in Fig. 6(d).

We argue that Fig. 6(a) shows modal field maps of the symmetric $p_x - p_x$ and antisymmetric $m_y - m_{y'}$ hybridized modes, respectively, for four reasons. (i) The calculated field profiles strongly resemble the corresponding measured intensity maps. The lack of high field intensity in the middle of the CL map for $\lambda = 450$ nm is attributed to the finite size of the electron beam and the strong local asymmetry in the field profile. To illustrate this, Fig. 6(d) shows the dipole orientation (left). At the center of the dimer, the E_z fields of the dipoles have an antiparallel orientation, which limits the excitation efficiency by the symmetric field of the electron beam. (ii) The symmetric $p_x - p_x$ ($\lambda = 450$ nm) bonding mode is strongly redshifted with respect to the p_x mode of the single particle ($\lambda = 430$ nm), which is consistent with earlier work [33]. The resonance wavelength for the $m_y - m_{y'}$ mode ($\lambda = 490$ nm), on the other hand, shows only a weak redshift compared to the single-particle m_y mode ($\lambda = 485$ nm). The relatively large and small spectral shifts are also consistent with those obtained from the calculated eigenfrequencies. (iii) The spatial intensity profile observed for $\lambda = 450$ nm (left) dominates the CL intensity maps over a large spectral range ($430 < \lambda < 480$ nm), while the spatial intensity profile observed for $\lambda = 490$ nm (right) is relatively weak and is only observed for a narrow spectral range. This is in agreement with previous work [33], which showed that the symmetric $p_x - p_x$ bonding mode dominates the scattering spectrum over a wide spectral range. (iv) The imaginary part of the calculated eigenfrequencies matches this trend: $\Im(f_{p_x - p_x}) = 148$ THz ($Q \sim 5$), which indicates large radiative losses as a result of the large effective dipole moment, corresponding to a large bandwidth. $\Im(f_{m_y - m_{y'}}) = 9$ THz ($Q \sim 65$), on the other hand, indicates weak radiative losses due to the weak coupling to plane waves as a result of the modal asymmetry, corresponding to a narrow line width. Altogether, Fig. 6 shows that CL can be used to directly map modal field profiles of both symmetric and antisymmetric hybridized eigenmodes.

C. Rectangular Dimers

Finally, to map hybridized eigenmodes with further increased complexity, we focus on a larger dimer structure that exhibits higher-order modes and more complex modal field profiles. The dimer is comprised of two rectangular bars with a 100 nm width and height, 300 nm length, and 35 nm spacing [see Fig. 7(b)]. These individual resonators have well-defined leaky resonances that can be described theoretically as modified Fabry–Perot modes [3].

The individual bars exhibit a large collection of geometrical modes as a result of their size, and each mode gives rise to a distinct resonant peak in the CL spectrum [Fig. 7(a), blue curve]. Coupling among the large number of modes results in a broad range of hybridized modes, giving rise to even more resonant peaks with strong spectral overlap [Fig. 7(a), red curve].

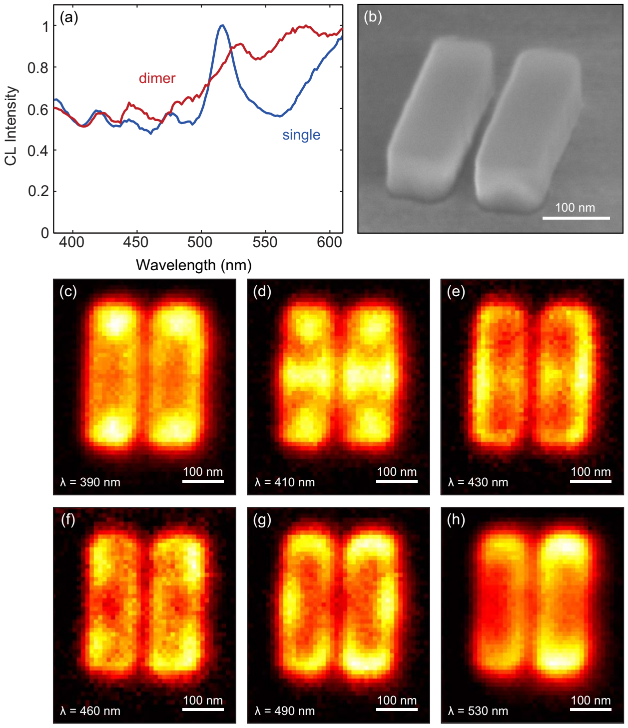

Fig. 7. (a) CL intensity spectrum for a single bar (blue) and dimer (red), (b) SEM image (imaged under 52°) of a dimer comprised of rectangular particles with 300 nm length, 100 nm width, and 100 nm height; the particle spacing is 35 nm. (c)–(h) Two-dimensional CL intensity map for (c) $\lambda = 390$ nm, (d) $\lambda = 410$ nm, (e) $\lambda = 430$ nm, (f) $\lambda = 460$ nm, (g) $\lambda = 490$ nm, and (h) $\lambda = 530$ nm, showing hybridization of higher-order eigenmodes.

Unlike DF spectroscopy or SNOM measurements, the modal field maps measured by CL imaging can be used to resolve the individual modes. We present six examples of CL intensity maps that unambiguously show field profiles of hybridized resonant modes. Figures 7(c)–7(h) display the measured mode maps for different wavelengths in the range $\lambda = 390$–530 nm, showing highly complex modal profiles inside the individual bars corresponding to higher-order modes. High field intensities at the center or outside of the dimer are a direct indication of hybridization. This example demonstrates how CL can be used to directly map complex hybridized field profiles inside single nanostructures, which allows for detailed characterization of resonant modes of coupled structures.

5. CONCLUSIONS

In conclusion, we have demonstrated direct imaging of hybridized eigenmodes in coupled resonant silicon nanoparticles. Using DF spectroscopy, we studied the influence of gap size on the scattering spectrum and showed strong spectral broadening as a result of mode hybridization. Using finite-element modeling, we analyzed the eigenmodes of the coupled nanoparticles and identified the hybridized modes that dominate the scattering spectrum. CL imaging spectroscopy was used to directly image the modal field profiles of individual and coupled nanoparticles with deep-subwavelength resolution, showing strongly hybridized field profiles. Detailed analysis of the CL results and eigenmode calculations showed that the measured modal field profiles correspond to the hybridized symmetric $p_x - p_x$ and antisymmetric $m_y - m_{y'}$ bonding modes. Finally, we studied dimers composed of large dielectric bars to explore the ability of CL imaging to map highly complex hybridized field profiles inside single resonant nanostructures. Our results demonstrate the ability to characterize the complex resonant properties of coupled nanostructures. Based on a detailed fundamental understanding of coupled resonators, nanostructures with accurately engineered field confinement and scattering profiles can be designed, paving the way for more complex structures and next-generation devices.

Funding. Dutch Ministry of Economic Affairs; European Research Council (ERC) (ERC267634); Nederlandse Organisatie voor Wetenschappelijk Onderzoek (NWO).

Acknowledgment. This work is part of the research program of the "Stichting voor Fundamenteel Onderzoek der Materie (FOM)" which is part of the "Nederlandse Organisatie voor Wetenschappelijk Onderzoek (NWO)". It is also supported by NanoNextNL, a nanotechnology program funded by the Dutch Ministry of Economic Affairs, and the European Research Council (ERC). A.P. is co-founder and co-owner of Delmic BV, a startup company that has developed a commercial product based on the cathodoluminescence system that was used in this work.

See Supplement 1 for supporting content.

REFERENCES

1. C. F. Bohren and D. R. Huffmann, *Absorption and Scattering of Light by Small Particles* (Wiley, 1983).
2. J. A. Schuller and M. L. Brongersma, "General properties of dielectric optical antennas," Opt. Express **17**, 24084–24095 (2009).
3. L. Huang, Y. Yu, and L. Cao, "General modal properties of optical resonances in subwavelength nonspherical dielectric structures," Nano Lett. **13**, 3559–3565 (2013).
4. L. Cao, J. S. White, J.-S. Park, J. A. Schuller, B. M. Clemens, and M. L. Brongersma, "Engineering light absorption in semiconductor nanowire devices," Nat. Mater. **8**, 643–647 (2009).
5. L. Cao, J.-S. Park, P. Fan, B. Clemens, and M. L. Brongersma, "Resonant germanium nanoantenna photodetectors," Nano Lett. **10**, 1229–1233 (2010).
6. J. C. Johnson, H.-J. Choi, K. P. Knutsen, R. D. Schaller, P. Yang, and R. J. Saykally, "Single gallium nitride nanowire lasers," Nat. Mater. **1**, 106–110 (2002).
7. X. Duan, Y. Huang, R. Agarwal, and C. M. Lieber, "Single-nanowire electrically driven lasers," Nature **421**, 241–245 (2003).
8. K. L. van der Molen, P. Zijlstra, A. Lagendijk, and A. P. Mosk, "Laser threshold of Mie resonances," Opt. Lett. **31**, 1432–1434 (2006).
9. P. Spinelli, M. A. Verschuuren, and A. Polman, "Broadband omnidirectional antireflection coating based on subwavelength surface Mie resonators," Nat. Commun. **3**, 692 (2012).
10. A. Raman, Z. Yu, and S. Fan, "Dielectric nanostructures for broadband light trapping in organic solar cells," Opt. Express **19**, 19015–19026 (2011).
11. S. A. Mann, R. R. Grote, R. M. Osgood, and J. A. Schuller, "Dielectric particle and void resonators for thin film solar cell textures," Opt. Express **19**, 25729–25740 (2011).
12. S.-K. Kim, R. W. Day, J. F. Cahoon, T. J. Kempa, K.-D. Song, H.-G. Park, and C. M. Lieber, "Tuning light absorption in core/shell silicon nanowire photovoltaic devices through morphological design," Nano Lett. **12**, 4971–4976 (2012).
13. A. García-Etxarri, R. Gómez-Medina, L. S. Froufe-Pérez, C. López, L. Chantada, F. Scheffold, J. Aizpurua, M. Nieto-Vesperinas, and J. J.

Sáenz, "Strong magnetic response of submicron silicon particles in the infrared," Opt. Express **19**, 4815–4826 (2011).
14. A. B. Evlyukhin, S. M. Novikov, U. Zywietz, R. L. Eriksen, C. Reinhardt, S. I. Bozhevolnyi, and B. N. Chichkov, "Demonstration of magnetic dipole resonances of dielectric nanospheres in the visible region," Nano Lett. **12**, 3749–3755 (2012).
15. A. I. Kuznetsov, A. E. Miroshnichenko, Y. H. Fu, J. Zhang, and B. Luk'yanchuk, "Magnetic light," Sci. Rep. **2**, 492 (2012).
16. M. K. Schmidt, R. Esteban, J. J. Sáenz, I. Suárez-Lacalle, S. Mackowski, and J. Aizpurua, "Dielectric antennas: a suitable platform for controlling magnetic dipolar emission," Opt. Express **20**, 13636–13650 (2012).
17. M. Kerker, D. S. Wang, and C. L. Giles, "Electromagnetic scattering by magnetic spheres," J. Opt. Soc. Am. **73**, 765–767 (1983).
18. S. Person, M. Jain, Z. Lapin, J. J. Sáenz, G. Wicks, and L. Novotny, "Demonstration of zero optical backscattering from single nanoparticles," Nano Lett. **13**, 1806–1809 (2013).
19. Y. H. Fu, A. I. Kuznetsov, A. E. Miroshnichenko, Y. F. Yu, and B. Luk'yanchuk, "Directional visible light scattering by silicon nanoparticles," Nat. Commun. **4**, 1527 (2013).
20. Q. Zhao, L. Kang, B. Du, H. Zhao, Q. Xie, X. Huang, B. Li, J. Zhou, and L. Li, "Experimental demonstration of isotropic negative permeability in a three-dimensional dielectric composite," Phys. Rev. Lett. **101**, 027402 (2008).
21. Q. Zhao, J. Zhou, F. Zhang, and D. Lippens, "Mie resonance-based dielectric metamaterials," Mater. Today **12**(12), 60–69 (2009).
22. J. C. Ginn, I. Brener, D. W. Peters, J. R. Wendt, J. O. Stevens, P. F. Hines, L. I. Basilio, L. K. Warne, J. F. Ihlefeld, P. G. Clem, and M. B. Sinclair, "Realizing optical magnetism from dielectric metamaterials," Phys. Rev. Lett. **108**, 097402 (2012).
23. P. Moitra, Y. Yang, Z. Anderson, I. I. Kravchenko, D. P. Briggs, and J. Valentine, "Realization of an all-dielectric zero-index optical metamaterial," Nat. Photonics **7**, 791–795 (2013).
24. S. Liu, M. B. Sinclair, T. S. Mahony, Y. C. Jun, S. Campione, J. Ginn, D. A. Bender, J. R. Wendt, J. F. Ihlefeld, P. G. Clem, J. B. Wright, and I. Brener, "Optical magnetic mirrors without metals," Optica **1**, 250–256 (2014).
25. D. Lin, P. Fan, E. Hasman, and M. L. Brongersma, "Dielectric gradient metasurface optical elements," Science **345**, 298–302 (2014).
26. T. Coenen, J. van de Groep, and A. Polman, "Resonant modes of single silicon nanocavities excited by electron irradiation," ACS Nano **7**, 1689–1698 (2013).
27. C. Wang, Z. Y. Jia, K. Zhang, Y. Zhou, R. H. Fan, X. Xiong, and R. W. Peng, "Broadband optical scattering in coupled silicon nanocylinders," J. Appl. Phys. **115**, 244312 (2014).
28. J. Yan, P. Liu, Z. Lin, H. Wang, H. Chen, C. Wang, and G. Yang, "Directional Fano resonance in a silicon nanosphere dimer," ACS Nano **9**, 2968–2980 (2015).
29. P. Albella, M. A. Poyli, M. K. Schmidt, S. A. Maier, F. Moreno, J. J. Sáenz, and J. Aizpurua, "Low-loss electric and magnetic field-enhanced spectroscopy with subwavelength silicon dimers," J. Phys. Chem. C **117**, 13573–13584 (2013).
30. R. M. Bakker, D. Permyakov, Y. F. Yu, D. Markovich, R. Paniagua-Domínguez, L. Gonzaga, A. Samusev, Y. Kivshar, B. Luk'yanchuk, and A. I. Kuznetsov, "Magnetic and electric hotspots with silicon nanodimers," Nano Lett. **15**, 2137–2142 (2015).
31. E. Prodan, C. Radloff, N. J. Halas, and P. Nordlander, "A hybridization model for the plasmon response of complex nanostructures," Science **302**, 419–422 (2003).
32. P. Nordlander, C. Oubre, E. Prodan, K. Li, and M. I. Stockman, "Plasmon hybridization in nanoparticle dimers," Nano Lett. **4**, 899–903 (2004).
33. U. Zywietz, M. K. Schmidt, A. B. Evlyukhin, C. Reinhardt, J. Aizpurua, and B. N. Chichkov, "Electromagnetic resonances of silicon nanoparticle dimers in the visible," ACS Photon. **2**, 913–920 (2015).
34. D.-S. Kim, J. Heo, S.-H. Ahn, S. W. Han, W. S. Yun, and Z. H. Kim, "Real-space mapping of the strongly coupled plasmons of nanoparticle dimers," Nano Lett. **9**, 3619–3625 (2009).
35. J. van de Groep and A. Polman, "Designing dielectric resonators on substrates: combining magnetic and electric resonances," Opt. Express **21**, 26285–26302 (2013).
36. COMSOL Multiphysics 5.0.
37. K. H. Drexhage, "Influence of a dielectric interface on fluorescence decay time," J. Lumin. **1–2**, 693–701 (1970).
38. T. Coenen, E. J. R. Vesseur, and A. Polman, "Angle-resolved cathodoluminescence spectroscopy," Appl. Phys. Lett. **99**, 143103 (2011).
39. T. Coenen, B. J. M. Brenny, E. J. R. Vesseur, and A. Polman, "Cathodoluminescence microscopy: optical imaging and spectroscopy with deep-subwavelength resolution," MRS Bull. **40**(04), 359–365 (2015).
40. R. Sapienza, T. Coenen, J. Renger, M. Kuttge, N. F. van Hulst, and A. Polman, "Deep-subwavelength imaging of the modal dispersion of light," Nat. Mater. **11**, 781–787 (2012).
41. E. J. R. Vesseur and A. Polman, "Plasmonic whispering gallery cavities as optical nanoantennas," Nano Lett. **11**, 5524–5530 (2011).
42. T. Coenen, E. J. R. Vesseur, and A. Polman, "Deep subwavelength spatial characterization of angular emission from single-crystal Au plasmonic ridge nanoantennas," ACS Nano **6**, 1742–1750 (2012).
43. E. J. R. Vesseur, T. Coenen, H. Caglayan, N. Engheta, and A. Polman, "Experimental verification of n = 0 structures for visible light," Phys. Rev. Lett. **110**, 013902 (2013).
44. T. Coenen, F. B. Arango, A. F. Koenderink, and A. Polman, "Directional emission from a single plasmonic scatterer," Nat. Commun. **5**, 3250 (2014).
45. T. Coenen and A. Polman, "Optical properties of single plasmonic holes probed with local electron beam excitation," ACS Nano **8**, 7350–7358 (2014).
46. F. J. García de Abajo, "Optical excitations in electron microscopy," Rev. Mod. Phys. **82**, 209–275 (2010).